

AUTOMATIC DETECTION OF BONE MARROW INFILTRATION BY MULTIPLE MYELOMA DETECTION IN LOW-DOSE CT

F. Martínez-Martínez, J. Kybic*

Czech Technical University in Prague,
Faculty of Electrical Engineering,
Department of Cybernetics,
Center for Machine Perception

L. Lambert†

Charles University in Prague,
First Faculty of Medicine,
Department of Radiology

ABSTRACT

Multiple myeloma is a disease primarily affecting bone marrow. This paper presents a novel method that can automatically detect infiltration of the bone marrow by multiple myeloma in diseased femurs (thigh bones) from low-dose CT images. This detection is done by evaluating two aspects of the CT images: bone marrow infiltrations (increased density values compared to regular fatty bone marrow) and scalloping (indentation of the inner margin of the cortical bone). First, bone marrow and cortical bone are automatically segmented from CT images. Afterwards, a probabilistic model of the bone marrow density is created in order to automatically detect islands of infiltrations. Finally, scalloping is detected by means of the quantification of the roughness of the boundary between the bone marrow and bony tissue. We have experimentally tested both infiltration and scalloping detection methods, obtaining a sensitivity of 74.9% and 69.2% and a specificity of 75% and 61% respectively.

Index Terms— Myeloma, scalloping, infiltration, automatic, detection

1. INTRODUCTION

Multiple myeloma is a disease characterized by the uncontrolled proliferation of malignant plasma cells that are typically located in the bone marrow [1]. Bone marrow therefore becomes infiltrated and osteolytic lesions may appear in form ranging from scalloped inner profiles of the cortical bone to large defects. Imaging of patients with multiple myeloma plays an important role in staging of the disease, together with laboratory finding and bone marrow biopsy. Multiple myeloma can be detected by two characteristics in the image: bone marrow infiltrations and scalloping. Infiltrations, which appear as increased density regions, can vary in size and shape

and scalloping is characterized by the indentation of the inner margin of the cortical bone (lytic lesions) (Figure 1).

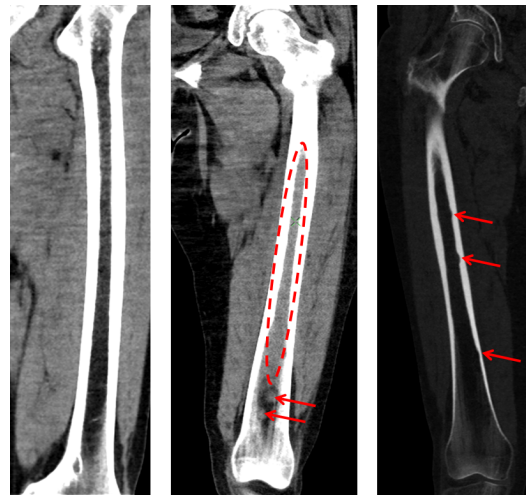


Fig. 1. Healthy femur (left), infiltrated femur (center) and femur with scalloping (right). A big infiltration is highlighted with a dashed ellipse and two small infiltration islands with arrows (center). The scalloping is also highlighted with arrows (right).

Conventional radiography (X-ray skeletal survey) has long been the gold standard in staging of skeletal involvement by multiple myeloma, which was reflected in the Durie-Salmon staging system. With the expansion of cross-sectional imaging, CT and MR have been validated for multiple myeloma and a new Durie-Salmon plus staging system devised [2, 3]. We have concentrated on CT because it is accessible, relatively cheap and faster than MR. Moreover, CT has an advantage in the evaluation of extrasosseous lesions. However, the radiation dose is higher and it has difficulties in assessment of bone marrow infiltration and differentiation between cellular and fatty bone marrow [4]. In this work we have used low-dose CT to decrease the radiation dose. However, the image quality is lower than in conventional

*F. Martínez-Martínez and J. Kybic have been supported by the Czech Science Foundation projects 14-10440S and 14-21421S respectively.

†The clinical part has been supported by PRVOK-P27/LF1 and OPPK CZ.2.16/3.1.00/24012

CT, which makes more challenging the detection of multiple myeloma from CT.

To the best of our knowledge, there are no automatic methods for the detection of multiple myeloma. Until now this task has been manually performed by radiologists. This work presents a methodology to automatically detect the presence of multiple myeloma in low-dose CT images of long bones, especially femur. Our algorithm first segments the bone marrow and the cortical bone and afterwards detects infiltrations in the bone marrow and scalloping of the cortical bone.

2. METHODS

2.1. Segmentation of bone marrow and cortical bone.

An algorithm to automatically segment the bone marrow and the cortical bone from the 3D CT images was implemented (Fig. 2). This algorithm binarizes each 2D slice image with a global threshold of 500 HU to obtain the cortical bone binary mask. This mask was flood filled and the interior of the bone (medular cavity) was found by the difference between the cortical bone mask and the flood filled mask. The interval of interest in the longitudinal axis comprises the diaphysis, from subtrochanteric region down to the distal metaphysis of the femur (Fig. 2 bottom).

2.2. Spatial alignment

After the segmentation, the two binary masks and the 3D images were cropped and split to get two separated femurs for each subject. Afterwards, Principal Component Analysis was performed on the 3D coordinates from the bone marrow voxels in order to estimate the principal direction of the femur. The split images and binary masks were rotated, so that the principal direction was aligned with the longitudinal axis using the method proposed in [5].

2.3. Infiltration detection

Infiltration of the bone marrow is characterized by islands or confluent areas of increased density values compared to regular fatty bone marrow density. However, simple thresholding is not sufficient to detect them, since the density in normal tissue is not uniform, increasing in the axial direction from the center towards the inner cortical layer, as well as in the longitudinal distal to proximal direction. For this reason, we decided to build a probabilistic model of the bone marrow density. The bone marrow voxels are grouped in sub-volumes taking into account this spatial dependency and their histograms are computed. Standard Euclidean coordinate $\mathbf{r}=(x,y,z)$ is mapped to accommodate differences in the femur sizes and shapes. In particular, \mathbf{r} is mapped to normalized longitudinal and radial coordinates $(l, h) \in [0, 1] \times [0, 1]$

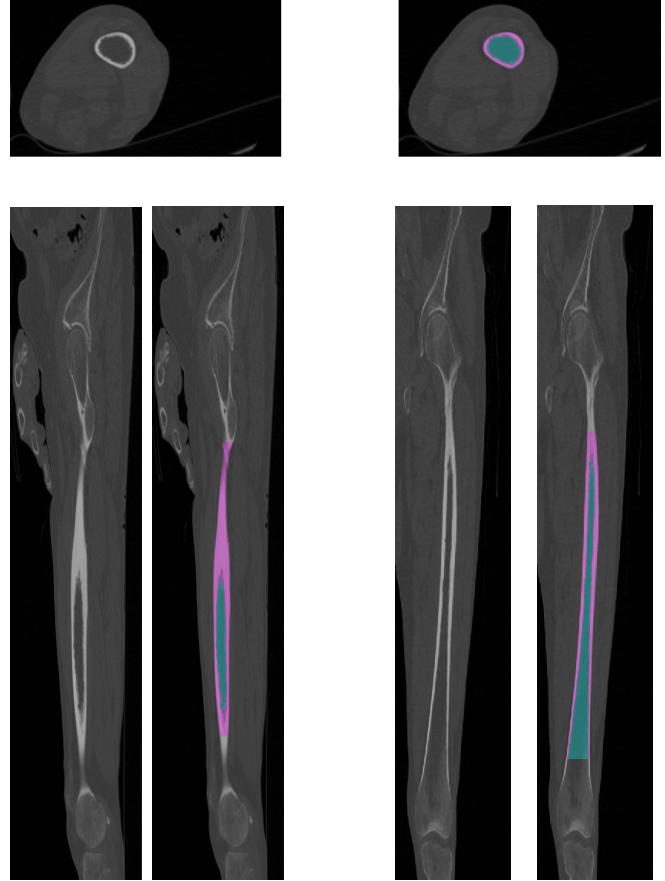


Fig. 2. Transversal (top), sagittal (bottom-left) and frontal (bottom-right) views of original CT slices from a femur (left) and slices with segmentations superimposed (right). The segmented bone marrow is showed in cyan while the segmented cortical bone in magenta.

defined below. In the z -direction (longitudinal axis) we simply normalize the position to $[0,1]$:

$$l = (z - z_{min}) / (z_{max} - z_{min}) \quad (1)$$

where z_{min} and z_{max} are limits of binary mask in the longitudinal axis (limits of the diaphysis). To calculate the radial coordinate, we go over all slices. In each one we find the centroid of the bone marrow binary mask and for each voxel \mathbf{r} from that slice we calculate the direction θ from the slice centroid to point \mathbf{r} . Then, we find the distance $u(\theta)$ from centroid to the mask boundary in the direction $u(\theta)$. The relative radial distance h then satisfies:

$$\begin{aligned} x &= hu(\theta) \sin \theta \\ y &= hu(\theta) \cos \theta \end{aligned} \quad (2)$$

Since only a limited number of training data was available, the model needed to be simple, with a small number of

degrees of freedom. The probabilistic model was built from a training set of healthy femurs. The voxels are grouped varying l and h coordinates with step sizes $\Delta_l = \Delta_h = 0.1$ obtaining 100 sub-volumes. The histograms of the density values from each sub-volume are calculated for each femur. Each histogram is constructed computing the frequency count of the density values using 513 bins in the range of [-1024 1024] HU. The histograms belonging the same sub-volume from all the training images are summed and the resulting histograms are interpolated by a factor of 4 using a cubic interpolation. The interpolated histograms have a bin for each density value in the range [-1024 1024] HU. Finally, the interpolated histograms are normalized to sum to 1. Figure 3 shows an example of 100 normalized histograms that represent the probabilistic model.

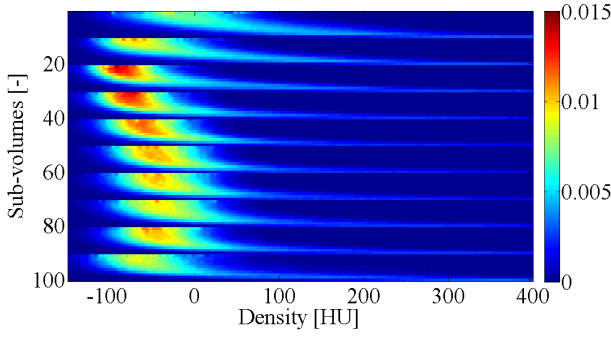


Fig. 3. An example of normalized histograms representing the probabilistic model estimated from a set of training images of healthy femurs: the histograms centered in lower density values with narrow deviation correspond to the inner layers of the bone marrow while the histograms centered in higher density values with wide deviation correspond to the outer layer of the bone marrow.

In a traditional computer aided diagnostic setting, we would also create a model for the diseased tissue and compare the likelihood of the two models. However, this is not practical for multiple myeloma involvement of femur, since there is a great variability in the appearance of the diseased bones (Fig. 1) and only a limited amount of training data is available. Instead, we detect outliers of the normal model, i.e. high intensity voxels which cannot be explained by the normal model. Given a voxel \mathbf{r} from a test image with coordinates (l, h) , we estimate by means of its corresponding normalized histogram the probability that the intensity I at this position be higher than the intensity of \mathbf{r} , $P[I \geq I(l, h)]$ (given (l, h)), under the hypothesis of the femur being normal. A voxel is considered an outlier if this probability is lower than a chosen threshold ζ_0 :

$$P[I \geq I(l, h)] < \zeta_0 \rightarrow \mathbf{r}(l, h) \in outlier \quad (3)$$

We consider a bone marrow to be abnormal if there are at

least ρ connected components each bigger than τ outliers.

2.4. Scalloping detection

We quantified the roughness of the boundary between bone marrow and bony tissue to detect scalloping. We started with the radial distance profile $u(\theta, z)$ mentioned above, where we have now added the so far implicit parameter z . We evaluate $u(\theta, z)$ for all slices inside the zone of interest and for $n_\theta = 100$ uniformly sampled angles θ .

One of the difficulties is that the changes we want to detect are very small, often around one voxel, so it is hard to use for example mathematical morphology. To obtain subpixel resolution, the profile $u(\theta, z)$ is reestimated by linear interpolation from neighboring pixels. In particular, we sample the interpolated version of the intensity in real coordinates, $f(\theta, z, q)$, for constant θ and z and varying q with step size $\Delta q = 0.1$, stopping as soon as $f(\theta, z, q) > T$, where $T = 700$ HU is the bone threshold. This threshold is higher than in the cortical bone segmentation (section 2.1) to avoid the creation of holes. If the boundary cannot be found, it is linearly interpolated from neighboring (z, q) .

We smooth $u(\theta, z)$ by Gaussian filtering in both θ and z , with standard deviations of the filter $\sigma_z = 20$ mm and $\sigma_\theta = 0.03$ rad, using circular boundary conditions for θ and constant boundary conditions for z . The roughness is then quantified by the squared difference ξ of the original u and the smoothed version. The difference is smoothed with another Gaussian filter of size $\sigma_\xi = 5$ pixels ≈ 5 mm to gain robustness.

$$\xi(\theta, z) = G_{\sigma_\xi} * (u(\theta, z) - u(\theta, z) * G_{\sigma_\theta} * G_{\sigma_z})^2 \quad (4)$$

Similarly to the infiltration detector, we consider the femur to be abnormal, if the roughness exceeds a threshold anywhere within the zone of interest, i.e. if $\max_{\theta, z} \xi(\theta, z) > \xi_0$ for $\theta \in (0, 2\pi)$, $z \in [z_s^+, z_s^-]$, where ξ_0 is a user-defined threshold. Based on preliminary experiments, the test interval $[z_s^+, z_s^-]$ for z is selected by eliminating the top and bottom 10% of the zone of interest, where the curvature of the medullary cavity walls increases and false positives due to high values of ξ would otherwise occur.

3. EXPERIMENTS

The study was approved by local Institutional Review Board and all patients signed an informed consent. The examinations were performed on a 256-slice scanner (Brilliance iCT 256; Philips Healthcare, Best, The Netherlands). The matrix size was 512×512 with a voxel size of $0.976 \times 0.976 \times 0.450$ mm. The acquisition was done in end-inspiration from vertex to knees (about 20s breath-hold).

Femurs from 135 subjects were examined: 92 healthy subjects and 43 subjects diagnosed with infiltrations of bone

marrow. From these 43 subjects, 18 had scalloping. The diagnosis was only available per subject and not per femur, so a subject was considered abnormal if any of its two femurs were abnormal. As explained in section 2.2, the images were split, obtaining a database with a total of 270 femurs.

A 5-fold cross-validation was performed to test the infiltration detection model. 4/5 of healthy femurs were used for training and the remaining 1/5 plus all the femurs from subjects with infiltrations were used for testing. In the case of scalloping detection, the model was tested on each subject independently. The roughness was calculated for each subject and compared with the threshold. The receiver operating characteristic (ROC) curves from both infiltration and scalloping detection models were obtained by varying the thresholds in order to optimize their performance (Fig. 4). Here ζ_0 , ρ and τ are the thresholds for the infiltration detection model and were varied between [0.001 0.4], [1 100] and [2 500] respectively. For the scalloping detection model the threshold ξ_0 was varied between [0 20].

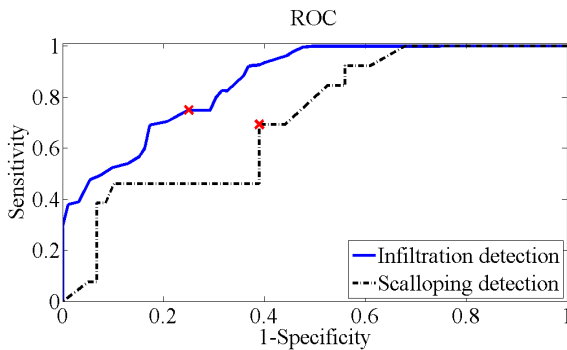


Fig. 4. Receiver operating characteristic curves from infiltration detection (continuous blue line) and scalloping detection (dashed black line). The red crosses indicate the selected classifiers, which correspond to the equal error rate.

The selected thresholds were $\zeta_0 = 0.002$, $\rho = 10$ connected component and $\tau = 5$ voxels for infiltration detection. For scalloping detection $\xi_0 = 1.23$. Table 1 shows the sensitivity and specificity provided by both models in the classification of subjects with infiltrations and scalloping.

Table 1. Results of the classification: values of sensitivity and specificity are given in % for the equal error rate for infiltration and scalloping detection.

	Infiltration	Scalloping
Sensitivity (%)	74.88 ± 2.81	69.23
Specificity (%)	75.00 ± 12.43	61.02

Figure 5 and 6 show the infiltration and scalloping detected by the models from two patients from the test set.

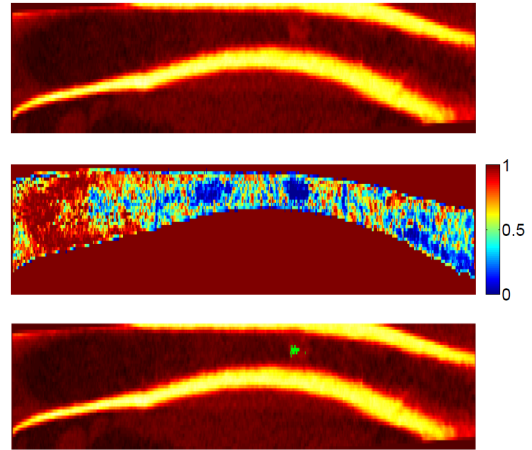


Fig. 5. Frontal view of the femur density from a subject with infiltration (top), estimated probabilities for each of the voxels from the bone marrow (middle) and the detected infiltration by the model with the selected thresholds in green color (bottom).

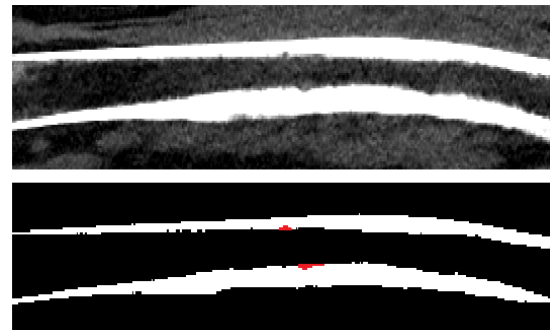


Fig. 6. Frontal view of the femur from a subject with scalloping (top) and cortical bone mask from with the detected scalloping in red (bottom).

4. DISCUSSION AND CONCLUSIONS

This paper has presented a method aimed at automatic detection of bone marrow infiltration and cortical scalloping of femurs in low-dose CT of patients with multiple myeloma. From the algorithmic point of view, both infiltration and scalloping detection can be implemented in linear time with respect to the number of bone marrow voxels, which should allow for a real time diagnostics. The most expensive operation is the Gaussian filtering, which can be efficiently parallelized.

This is the first step in creating a CAD system for myeloma detection from CT images. We expect the performance to improve in the future.

5. REFERENCES

- [1] M. E. Mulligan and A.Z. Badros, "PET/CT and MR imaging in myeloma," *Skeletal Radiol.*, vol. 36, no. 1, pp. 5–16, 2007.
- [2] A. H. Mahnken, J. E. Wildberger, G. Gehbauer, T. Schmitz-Rode, M. Blaum, U. Fabry, and R. W. Gunther, "Multidetector CT of the spine in multiple myeloma: comparison with MR imaging and radiography," *AJR Am J Roentgenol.*, vol. 178, no. 6, pp. 1429–36, 2002.
- [3] M. Horger, C.D. Claussen, U. Bross-Bach, R. Vonthein, T. Trabold, M. Heuschmid, and C. Pfannenber, "Whole-body low-dose multidetector row-CT in the diagnosis of multiple myeloma: an alternative to conventional radiography," *Eur J Radiol.*, vol. 54, no. 2, pp. 289–97, 2005.
- [4] C. J. Hanrahan, C. R. Christensen, and J. R. Crim, "Current concepts in the evaluation of multiple myeloma with MR imaging and FDG PET/CT," *Radiographics*, vol. 30, no. 1, pp. 127–42, 2010.
- [5] T. Moller and J. F. Hughes, "Efficiently building a matrix to rotate one vector to another," *Journal of Graphics Tools*, vol. 4, no. 4, pp. 2–4, 1999.